Robotica (2026), **44**, pp. 965–987
doi:10.1017/S0263574725102774

CAMBRIDGE UNIVERSITY PRESS

RESEARCH ARTICLE

Thermal point cloud-enhanced potential field path planning for mobile robots in high-temperature environments

Yunzhi Li[1], Libin Tan[1], Xiangrong Xu[1] and Zequn Zhang[2]

[1]Anhui University of Technology, Maxiang Road, Ma'anshan, Anhui, China
[2]Nanjing University of Aeronautics and Astronautics, 29 Yudao Street, Nanjing, Jiangsu, China
Corresponding author: Libin Tan; Email: alextlb@ahut.edu.cn

Received: 18 April 2025; **Revised:** 25 August 2025; **Accepted:** 1 October 2025; **First published online:** 11 May 2026

Keywords: mobile robot; LiDAR; thermal imager; potential field method; path planning

Abstract

This paper addresses the challenge of robotic path planning in high-temperature operational environments. Aiming at the limitation of traditional methods that rely on geometric information while ignoring thermal radiation data, a potential field method path planning based on temperature-enhanced point cloud maps is proposed. By fusing the data of LiDAR and thermal imager, point cloud maps with temperature attributes are generated. Based on the traditional potential field method, the potential field function of thermal radiation repulsion was introduced. The temperature gradient of the heat source is transformed into the potential energy constraint of path planning to achieve path generation in high-temperature areas. The experimental results show that, compared with the traditional artificial potential field method, this study provides a new technical solution for the safe operation of robots in a thermal environment.

1. Introduction

Path planning, as a cornerstone of autonomous robotics [1], faces critical challenges in high-temperature environments such as industrial inspection and fire rescue missions. Traditional path-planning methods mostly rely on geometric obstacle information [2, 3], which makes it difficult to avoid the risk of thermal damage. However, most of the existing research on fusion thermal imaging focuses on target detection [4, 5, 6]. The traditional path-planning method lacks the fusion of thermal information, so it is difficult to effectively avoid the high-temperature area or actively locate the heat source target. The fusion of LiDAR and thermal imager can provide multi-dimensional information on the geometry and thermal radiation for environmental modeling, but few existing path-planning algorithms make full use of thermal data.

Recent advancements in multimodal sensing have significantly expanded robotic perception capabilities. LiDAR and thermal imagers that can quickly sense environmental information have been widely studied. Douadi et al. [7] present a new feature-based approach for place recognition using 2D LiDAR data, which proposes a key point selection strategy to model places with persistent key points from concatenated LiDAR scans. Chen et al. [8] propose a novel approach by tightly coupling perception data from a thermal infrared camera and a LiDAR based on the advantages of the former. Wei et al. [9] introduce an innovative approach to 3D environmental mapping through the integration of a compact, handheld sensor package with a two-stage sensor fusion pipeline. The combination of radar and thermal imager can obtain rich environmental information and adapt to different mission requirements.

© The Author(s), 2026. Published by Cambridge University Press.

https://doi.org/10.1017/S0263574725102774 Published online by Cambridge University Press

How to use multimodal sensory data for path planning has also been extensively studied. The potential field method is a popular approach for path planning due to its simplicity and efficiency. Mantegh et al. [10] introduce a novel environment representation method that utilizes the Boundary Integral Equation method to map the environment into continuous Harmonic potential fields. Zhang et al. [11] propose a path-planning method based on "domain" for multiple underwater unmanned vehicles in a three-dimensional environment. Tong et al. [12] propose a new method of hybrid formation path planning based on A^* and a multi-target improved artificial potential field algorithm that provides the optimal collision-free path and improves the efficiency of multirobot formation path planning. The traditional potential field method mostly considers the geometric obstacle information and seldom considers the influence of thermal radiation on the path.

To solve these limitations, a potential field method based on temperature-enhanced point cloud maps is proposed in this paper to realize path planning in a thermal environment. The main contributions of this work are as follows:

1. Temperature-enhanced point cloud map construction: a fusion method for LiDAR and thermal imaging data is proposed to generate point cloud maps with thermal information.
2. Improved potential field function: based on the traditional artificial potential field method, the repulsive potential field function of heat radiation is introduced to realize the path planning of the robot in the environment with the heat source.
3. Experimental validation: the reliability of the proposed method is verified by collecting environmental data and conducting experiments.

The remainder of this paper is organized as follows. Section 2 presents some related work. Section 3 introduces the construction of thermal point cloud maps and presents the improved potential field function design. Section 4 provides experimental results and analysis. Finally, Section 5 concludes the paper and discusses future work.

2. Related work

Path planning for mobile robots has been extensively studied in the literature, with various approaches proposed to address different environmental challenges. In recent years, the integration of multimodal sensor data, particularly LiDAR and thermal imaging, has gained increasing attention due to its potential to enhance environmental perception and navigation robustness. This section reviews related works in two areas.

2.1. SLAM with LiDAR and thermal imager

At present, LiDAR-based SLAM has made great progress, which employs LiDAR for efficient map construction. Chen et al. [13] focus on localization and mapping issues for autonomous mobile robots equipped with low-cost 2D LiDAR in complex environments. A cross-correction LiDAR SLAM method [14] is proposed for constructing high-accuracy 2D maps of problematic scenarios. Yuan et al. [15] present SDV-LOAM, which incorporates semi-direct visual odometry and an adaptive sweep-to-map LiDAR odometry to effectively avoid the abovementioned errors and, in turn, achieve high tracking accuracy. A low-cost and portable indoor 3D mapping approach using biaxial line laser scanners and a one-dimensional laser range finder integrated with microelectromechanical systems is proposed [16]. Ali et al. [17] propose a feature-based SLAM algorithm using 2D image projections of the 3D laser point cloud. Pierzchała et al. [18] propose the use of a Simultaneous Localization and Mapping algorithm, called graph-SLAM, to generate local maps of forests.

The ability to produce maps with infrared radiometric information is of great interest for many applications. Lu and Lu [5] propose a framework to estimate the scene depth directly from a single thermal

https://doi.org/10.1017/S0263574725102774 Published online by Cambridge University Press

image that can still observe the scene in low lighting conditions. De Pazzi et al. [19] present a system for large-scale thermal mapping based on IR thermal images and 3D LiDAR point cloud data fusion. Rho et al. [6] propose a method of point cloud generation for indoor low-visibility disaster environments. Shin and Na [20] present an algorithm that displays the elevation and temperature of a surveillance area in the form of a map using a mobile robot platform equipped with LiDAR and a thermal imaging camera and determines whether it is abnormal. Krishnan [21] investigates the problem of fusing information from a LiDAR, a color camera, and a thermal camera to build RGB-Depth-Thermal maps and presents an algorithm that solves a non-linear optimization problem to compute the relative pose between the cameras and the LiDAR.

2.2. Path planning by the artificial potential field method

The artificial potential field method abstracts the motion of the robot in the surrounding environment into a kind of artificial gravitational field. The target point produces "gravity", the obstacle produces "repulsion", and the movement of the mobile robot is controlled by seeking the resultant force. It is widely used in path-planning research because its path is smooth and safe.

Montiel et al. [22] propose a new method called Bacterial Potential Field, computing optimal paths in environments with static and dynamic obstacles for a mobile robot. Rasekhipour et al. [23] introduce a model predictive path-planning controller such that its objective includes potential functions along with the vehicle dynamics terms. Sun et al. [24] propose the artificial potential field grid method, considering the 3D path-planning applications of unmanned underwater vehicles. Cui et al. [25] propose a novel method, named QuatAPF, for DSMVs to facilitate safe and energy-efficient motion under intricate underwater environments. Pan et al. [26] propose an effective improved artificial potential function-based path-planning approach for multi-UAV systems, considering the local minimum of artificial potential function. Wu et al. [27] propose an improved APF algorithm with road boundary function constraints in the path pre-planning layer, considering path pre-planning and re-planning. Ma et al. [28] propose a driving potential field model to improve the autonomy, safety, and comfort of CAVs during overtaking. To address the goals that are non-reachable with obstacles near issues of the artificial potential field, Gu et al. [29] propose an adaptive and secure path-planning method by incorporating a smooth decay function into the repulsive potential field. To enhance the roll stability on off-road terrain, Liu et al. [30] present a 3D gradient reconstruction-based path-planning method. Aiming at the formation and path planning of multirobot systems in an unknown environment, Fan et al. [31] propose a path-planning method for multirobot formation based on improved Q-learning. Cao et al. [32] propose a multifaceted approach to three-dimensional trajectory planning based on the combination of Rapidly-exploring Random Tree-Connect algorithm and artificial potential field method.

Although potential field methods have been extensively studied for real-time navigation, their adaptation to thermal point cloud maps remains underexplored. According to the characteristics of 2D LiDAR and thermal imager, a potential field method path-planning algorithm based on temperature-enhanced point cloud maps is proposed in this paper.

3. The proposed model

2D LiDAR can map quickly and accurately, which can only reflect the physical characteristics of the environment. Thermal imaging cameras can obtain thermal information about the external environment, but the perception of the physical environment is limited. Therefore, considering the limitations of a single sensor, this paper fuses the two into a 2D point cloud map with thermal information. On this basis, a path-planning method of artificial potential field combined with thermal information is proposed in this paper.

The principle of the framework is shown in Figure 1. Firstly, the internal and external parameters of the two sensors are obtained by the joint calibration method according to the obtained environmental

https://doi.org/10.1017/S0263574725102774 Published online by Cambridge University Press

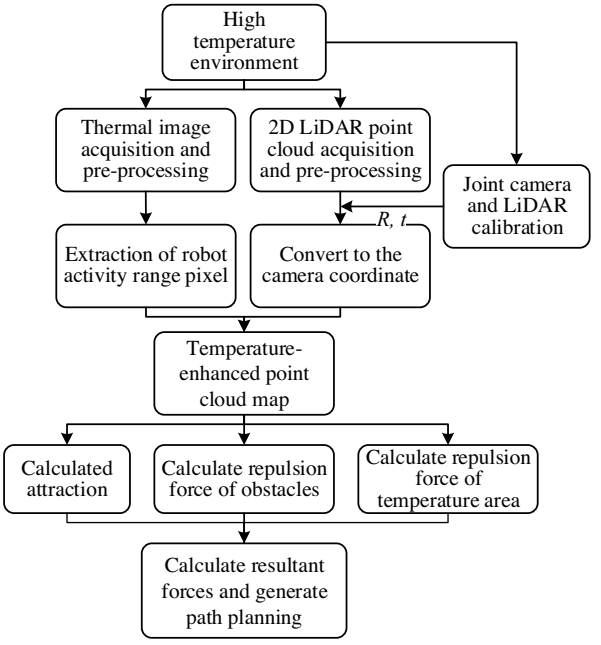


Figure 1. *Framework of the method.*

information. The data obtained by the two sensors is then preprocessed. At the same time, the 2D LiDAR point cloud is converted to camera coordinates after pre-processing. Since the images obtained by the camera cannot be fused directly with the LiDAR, the camera point cloud is projected onto the camera's imaging plane. Find the nearest pixel for each point cloud, add thermal information to the point cloud, and build a temperature-enhanced point cloud map. Attraction, repulsion, and temperature repulsion are calculated, respectively, to construct the overall map's field of influence based on this point cloud map. The final path planning is realized according to the force of the force field on the robot.

3.1. Thermal imager and LiDAR fusion mapping

3.1.1. Joint calibration

The data obtained by 2D LiDAR and thermal imager are based on their respective coordinate systems. In order to realize the data fusion of 2D LiDAR and thermal imager, it is necessary to unify their data into the same coordinate system, and the key is to determine the rigid coordinate transformation relationship between the two sensors.

Suppose one point $\boldsymbol{P}$ is $\boldsymbol{P}_l = (X_l, Y_l, Z_l)^T$ in the 2D LiDAR coordinate system and is $\boldsymbol{P}_t = (X_t, Y_t, Z_t)^T$ in the thermal imager coordinate system. The relation between $\boldsymbol{P}_l$ and $\boldsymbol{P}_t$ can be expressed as

$$\boldsymbol{P}_c = \begin{pmatrix} X_c \\ Y_c \\ Z_c \end{pmatrix} = \boldsymbol{R}\boldsymbol{P}_l + \boldsymbol{t} = \boldsymbol{R} \begin{pmatrix} X_l \\ Y_l \\ Z_l \end{pmatrix} + t. \tag{1}$$

where $\boldsymbol{R}$ and $\boldsymbol{t}$ are the rotation matrix and the offset matrix of the LiDAR coordinate system and the thermal imager coordinate system. The coordinate information of the camera space point can be represented by the pixel coordinate of the projection point (u, v) and the depth value Z_c of the corresponding projection point. The conversion relationship between $\boldsymbol{P}_l$ and camera pixel coordinates can be expressed as

https://doi.org/10.1017/S0263574725102774 Published online by Cambridge University Press

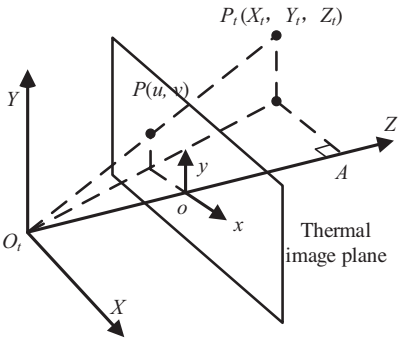


Figure 2. *Camera 3D point cloud projection.*

$$\begin{pmatrix} u \\ v \\ 1 \end{pmatrix} = \frac{1}{Z_c}\begin{pmatrix} f_x & 0 & c_x \\ 0 & f_y & c_y \\ 0 & 0 & 0 \end{pmatrix}\begin{pmatrix} X_c \\ Y_c \\ Z_c \end{pmatrix} = \frac{1}{Z_c}\boldsymbol{K}\begin{pmatrix} X_c \\ Y_c \\ Z_c \end{pmatrix} = \frac{1}{Z_c}\boldsymbol{K}\left(\boldsymbol{R}\begin{pmatrix} X_l \\ Y_l \\ Z_l \end{pmatrix} + \boldsymbol{t}\right). \tag{2}$$

where f_x and f_y are the focal length of the camera, c_x and c_y are the offset of the pixel coordinate system, $\boldsymbol{K}$ is the internal parameter matrix of the camera. The goal of joint calibration is to determine $\boldsymbol{K}$, $\boldsymbol{R}$, and $\boldsymbol{t}$.

3.1.2. Coordinate transformation

After coordinate transformation, LiDAR and thermal imager are in the same coordinate system. In order to fuse the camera point cloud and LiDAR point cloud, the radar point cloud needs to be projected onto the plane where the thermal imager map is located, as shown in Figure 2.

The coordinates of the points projected by the LiDAR point cloud onto the plane of the thermal imager map are expressed as

$$\begin{cases} u = \dfrac{f_x * X_c}{Z_c} + c_x \\ v = \dfrac{f_y * Y_c}{Z_c} + c_y \end{cases}. \tag{3}$$

The mismatch between the higher resolution of the thermal imaging image and the point cloud formed by the LiDAR is projected onto the image. This results in the LiDAR point cloud after projection being relatively sparse on the thermal imaging image. To extract temperature values from the thermal imaging image, we need to associate each LiDAR point with a pixel in the thermal imaging image. For each projection point of a single scan, the neighborhood range of the point is expanded to obtain more temperature information. After removing points that are beyond the image boundaries or have invalid depth, for each projection point of a single scan, the neighborhood range is expanded to obtain more temperature information. A circular neighborhood is extracted centered on the projection point (u, v), and the Euclidean distance of all pixels within the neighborhood to (u, v) is calculated.

$$d_k = \sqrt{(i_k - u)^2 + (j_k - v)^2}. \tag{4}$$

The temperature value t_k is extracted from the selected pixel set, and the average value t is calculated.

$$\begin{cases} t = \dfrac{\sum_{k=1}^{n} w_k * t_k}{\sum_{k=1}^{n} w_k} \\ w_k = exp\left(-d_k^2/\sigma^2\right) \end{cases}. \tag{5}$$

https://doi.org/10.1017/S0263574725102774 Published online by Cambridge University Press

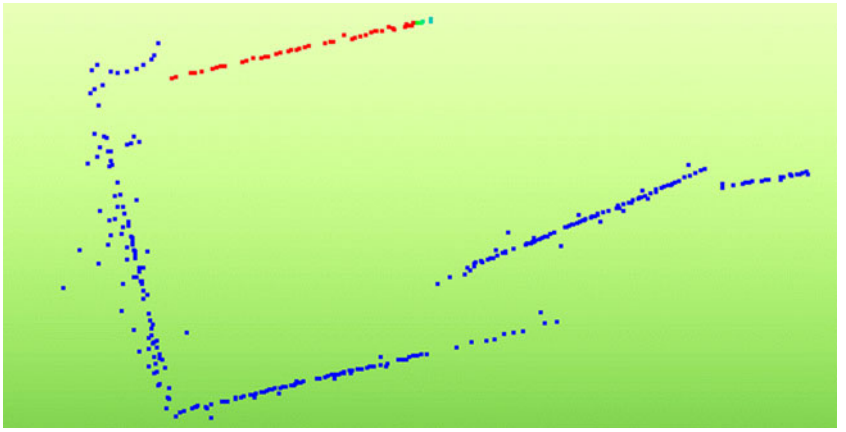


Figure 3. *Temperature-enhanced point cloud after sensor fusion.*

The temperature value t of the projection point is obtained through Gaussian weighted averaging. The weight w_k is an exponential decay function of the distance from the pixel to the center point. The closer the distance, the greater the weight. The parameter σ controls the speed of the decay.

The temperature value t of these hot spots is added to the original coordinates of the point cloud projection point, denoted as $\boldsymbol{P}_{tl} = (X_l, Y_l, Z_l, T)$.

The result after superposition fusion is shown in Figure 3. The laser point cloud data and pixel images of the thermal imager are obtained in the same coordinate system by conversion. The data from the two sensors are superimposed and used for building temperature-enhanced point clouds.

Due to the different data collection frequencies of LiDAR and thermal imagers, time synchronization is required before fusion. This can be achieved through timestamp alignment. Timestamps are recorded for each LiDAR scan and thermal image frame. For each LiDAR scan frame, the thermal image frame with the closest timestamp is found.

$$T_{\text{sync}} = arg \min_{\Delta t} \parallel P_{\text{lidar}}(t) - P_{\text{thermal}}\,(t + \Delta t) \parallel \tag{6}$$

When T_{sync} is less than the set value, data fusion is performed. If no synchronized frame is found, skip this LiDAR scan.

3.1.3. Loop closure detection in hot environments

The temperature-enhanced point cloud obtained by fusing thermal images and LiDAR sensors is used for closed-loop detection, which is applied to enhance the robustness, accuracy, and scene adaptability of the SLAM system, especially in the high-temperature environment described in this paper. During the robot's movement, inevitable mapping accumulation errors will occur. The closed-loop detection identifies loops to provide a strong constraint for the system, pulling the current pose and historical poses together, thereby significantly correcting the global consistency of the entire trajectory and map.

In this part, we propose to use geometric-thermal joint features for the closed-loop detection part. Features of 2D LiDAR point clouds and thermal imaging data are extracted to construct geometric-thermal joint feature descriptors.

In 2D point clouds, we usually calculate geometric features using points and their neighborhoods. Here, we adopt an algorithm similar to Fast Point Feature Histogram (FPFH), but simplify it to 2D. For point $\boldsymbol{p}$ and one of its neighboring points $\boldsymbol{q}_n$, the following characteristics are calculated.

- The angle α between the vector $\boldsymbol{pq}_n$ and the tangent vector at point $\boldsymbol{p}$ is obtained through local linear fitting within the domain.

https://doi.org/10.1017/S0263574725102774 Published online by Cambridge University Press

- The angle β between the tangent vector at point $\boldsymbol{q}_n$ and vector $\boldsymbol{pq}_n$.
- The angle θ between the normal vectors at point $\boldsymbol{p}$ and point $\boldsymbol{q}_n$.

Then, the angle features (α, β, θ) between point $\boldsymbol{p}$ and each of its neighboring points are statistically analyzed to form a histogram. Each angle is divided into several intervals, and the frequency of falling into each interval is counted. Thus, each point has a geometric feature histogram. This histogram is the simplified FPFH feature of the point, which we denote as $F_{\text{geom}}(\boldsymbol{p})$.

For each point $\boldsymbol{p}$, not only does it have its geometric information, but thermal imaging data is fused to attach a temperature value t to each point. Therefore, the following thermal features of point $\boldsymbol{p}$ and its domain point $\boldsymbol{q}_n$ are extracted.

– The average temperature of the neighborhood is as follows.

$$\mu_t = (1/k) * \sum t_i \tag{7}$$

i is the index of the neighborhood points, including point $\boldsymbol{p}$ itself.

– The standard deviation of the neighborhood temperature is as follows.

$$\sigma_t = \sqrt{(1/k) * \sum (t_i - \mu_t)^2} \tag{8}$$

– Divide the temperature range into several intervals, count the number of points in each temperature interval within the neighborhood, and form a neighborhood temperature distribution histogram, denoted as $hist_t$.

These three parts combine to form a thermal feature vector $F_{\text{thermal}}(\boldsymbol{p}) = [\mu_t, \sigma_t, hist_t]$.

The geometric feature histogram $F_{\text{geom}}(\boldsymbol{p})$ and the histogram $hist_t$ in the thermal feature are also normalized. μ_t and σ_t are standardized using the temperature mean and standard deviation of the entire scene.

$$\begin{cases} \mu_{\text{global}} = (1/N) * \sum t_i \\ \sigma_{\text{global}} = \sqrt{(1/N) * \sum (t_i - \mu_{\text{global}})^2} \\ \mu_t' = (\mu_t - \mu_{\text{global}})/\sigma_{\text{global}} \\ \sigma_t' = \sigma_t/\sigma_{\text{global}} \end{cases} \tag{9}$$

μ_{global} is the global average temperature, and σ_{global} is the global temperature standard deviation.

The normalized geometric features and thermal features are combined into a descriptor $F(\boldsymbol{p})$.

$$F(p) = \left[F'_{\text{geom}}(p), F'_{\text{thermal}}(p)\right] \tag{10}$$

Suppose that the key frame k contains N points. The global descriptor obtained by averaging the descriptors of the N points in the key frame can be expressed as follows.

$$G(k) = 1/N * \sum_{i=1}^{N} F(p_i) \tag{11}$$

For key frames k and c, calculate their global descriptors, respectively. Split the global descriptors into geometric and thermal parts as follows.

$$\begin{cases} G(k) = \left[G_{\text{geom}}(k), G_{\text{thermal}}(k)\right] \\ G(c) = \left[G_{\text{geom}}(c), G_{\text{thermal}}(c)\right] \end{cases} \tag{12}$$

Then, the geometric and thermal Euclidean distances are calculated separately as follows.

$$\begin{cases} d_g = \left\| G_{\text{geom}}(k) - G_{\text{geom}}(c) \right\|_2 \\ d_t = \left\| G_{\text{thermal}}(k) - G_{\text{thermal}}(c) \right\|_2 \end{cases} \tag{13}$$

https://doi.org/10.1017/S0263574725102774 Published online by Cambridge University Press

Set the geometric distance threshold τ_g and the thermal distance threshold τ_t. When the following conditions are simultaneously satisfied $d_g < \tau_g$ and $d_t < \tau_t$, then it is considered that the two key frames have passed the geometric-thermal consistency verification, that is, they are matched.

This method decomposes the global descriptors to independently verify the geometric and thermodynamic consistency, thereby avoiding incorrect matches in the dynamic thermal environment. Closed-loop detection of the fused thermal image and LiDAR can construct a more accurate and robust, globally consistent map.

3.2. Path planning with thermal map

3.2.1. Temperature-enhanced point cloud pretreatment

Due to the influence of hardware characteristics and detection noise, the temperature-enhanced point cloud obtained by LiDAR in thermal environment has the following problems: (1) The density of point cloud attenuates with the increase of detection distance, resulting in the overfitting of the temperature field at the near end and the loss of the features at the far end, which directly affects the accuracy of the temperature repulsion force; (2) Abnormal temperature value is introduced by sensor noise and environmental thermal disturbance, which is easy to cause path oscillation when directly used in repulsive field calculation; (3) The computational complexity of potential fields involving high-density discrete point clouds is high, which affects the computational efficiency of mobile robots. In order to alleviate the negative impact of the above problems on path generation, this paper adopts the grid method to preprocess the original point cloud.

The continuous two-dimensional space is divided into grids by fixed side lengths, each grid is identified by its index (i, j), and the central coordinate of each grid is calculated as the representative position. Each grid may contain multiple obstacle points, and the mean temperature of all points within the grid needs to be aggregated into a representative value.

$$T_{\text{grid}} = \frac{1}{N} \sum_{k=1}^{N} T_{ob,N} \tag{14}$$

If there are point clouds within the grid, each grid will be regarded as a circular obstacle. Its influence radius covers the entire grid area, ensuring that a path can be found by avoiding the grid edges.

$$R_{\text{grid}} = \frac{\sqrt{(\Delta x)^2 + (\Delta y)^2}}{2} = \frac{\sqrt{2}}{2} * L_{\text{grid}} \tag{15}$$

where $\Delta x = \Delta y = L_{\text{grid}}$ is the side length of the grid.

Due to the closed or obstructive environment, the intensity of the heat radiated by the high-temperature grid points to the surrounding space follows the exponential attenuation model in this paper. For a single high-temperature grid heat source $HS(x_s, y_s, T_s)$, the temperature value at which its thermal radiation decays to any grid (x, y) is

$$T(x, y) = \begin{cases} T_s \cdot e^{-\lambda \cdot d(x,y)} & \text{if } d(x, y) \le r \\ 0 & \text{otherwise} \end{cases} \tag{16}$$

Among them, λ is the speed of temperature diffusion controlled by the attenuation coefficient, and $d(x, y) = \sqrt{(x - x_s)^2 + (y - y_s)^2}$ is the distance from the target point to the heat source point. r is the effective radiation radius of the heat source. Beyond this range, it is considered to have no effect. If the target point is affected by multiple high-temperature grids, its temperature values are superimposed according to the radiation intensity.

This method can reduce the uncertainty of environmental modeling and provide a feasible framework for temperature sensing path planning, and its practical effect will be verified in subsequent experiments.

https://doi.org/10.1017/S0263574725102774 Published online by Cambridge University Press

3.2.2. Artificial potential field

The artificial potential field method is a common method for local path planning. It is the movement of the robot in the surrounding environment, designed as an abstract artificial gravitational field movement. The target point produces "gravity" in the mobile robot, and the obstacle produces "repulsion" in the mobile robot. Finally, the motion of the mobile robot is controlled by finding the resultant force.

The artificial potential field method models the environment as a potential field. The target point is attractive to the robot, and the potential field function can be expressed as

$$U_{\text{att}}(q) = \frac{1}{2} k_{att} \cdot d\left(q, q_{\text{goal}}\right)^2. \tag{17}$$

where q is the current position of the robot, q_{goal} is the target point, and k_{att} is the attraction coefficient.

Obstacles generate a repulsive force on the robot, and the potential field function can be expressed as

$$U_{\text{rep}}(q) = \begin{cases} \frac{1}{2} k_{\text{rep}} \cdot \left(\frac{1}{d\left(q, q_{\text{obs}}\right)} - \frac{1}{d_0}\right)^2 d^2\left(q, q_{\text{goal}}\right) & \text{if } d\left(q, q_{\text{obs}}\right) \le d_0 \\ 0 & \text{otherwise} \end{cases}. \tag{18}$$

where q_{obs} is the position of the obstacle, d_0 is the influence range of the obstacle, and k_{rep} is the repulsive force coefficient. The repulsive force of the obstacle does not always exist, but only occurs when the distance between the obstacle and the robot is less than the distance threshold.

3.2.3. Path planning with thermal information

By integrating the thermal information into the potential field method, the high-temperature area is regarded as an obstacle to increasing the repulsive force, and the potential field strength is dynamically adjusted according to the gradient distribution of the thermal value.

The point cloud data is converted into a raster map, and the thermal value T is assigned to each raster. The repulsive potential field in the high-temperature region can be expressed as

$$U_{\text{heat-rep}}(q) = \begin{cases} \frac{1}{2} k_{\text{heat-rep}} \cdot \frac{T\left(q_{\text{heat}}\right) - T_{\text{thre}}}{\max\left(d\left(q, q_{\text{heat}}\right)^2, d^2_{\text{heat- min}}\right)} & \text{if } T\left(q_{\text{heat}}\right) \ge T_{\text{thre}} \\ 0 & \text{otherwise} \end{cases}. \tag{19}$$

where $k_{\text{heat-rep}}$ is the coefficient of thermal repulsion force, $T(q)$ is the thermal value of the high-temperature region, and T_{thre} is the threshold of the high-temperature region. $k_{\text{heat-rep}}$ will adjust according to the range and importance of the thermal value and need to coordinate with the repulsive force of the obstacle to avoid conflict. The repulsive force weight is reduced at high temperatures near the target point, as follows.

$$k_{\text{heat-rep}} = k_{\text{heat-rep-base}} \left(1 - e^{-\frac{d\left(q, q_{\text{goal}}\right)^{\beta}}{2}}\right). \tag{20}$$

β is the attenuation coefficient that controls how fast the repulsive force decays as it approaches the target. The temperature-repulsive force of the obstacle is generated only when the distance between the obstacle and the robot is less than the threshold of temperature action. Based on the empirical formula of temperature decay with distance

$$T_d = T_0 * e^{-d/\alpha} \tag{21}$$

where T_0 is the temperature of the heat source and T_d is the temperature at a distance d from the heat source. By substituting T_{thre} into T_d, the distance between the temperature threshold and the heat source can be expressed as

$$D_{\text{thre}} = \alpha * (\ln T_0 - \ln T_{\text{thre}}) \tag{22}$$

https://doi.org/10.1017/S0263574725102774 Published online by Cambridge University Press

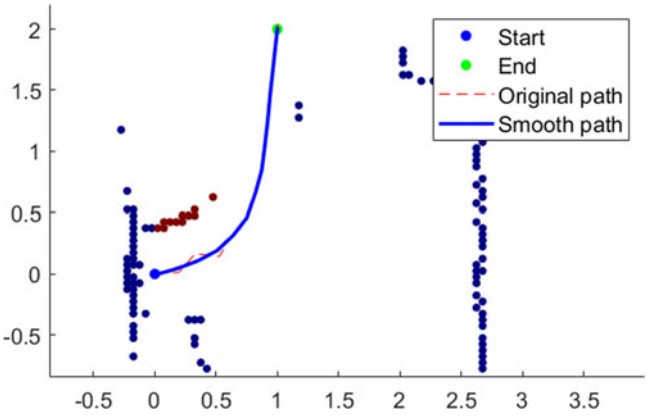


Figure 4. *The original path and smooth path are represented by the red dotted line and the blue solid line, respectively.*

The temperature-repulsive force of the obstacle only acts when the distance from the heat source is less than D_{thre}.

After superimposing all potential fields, the total potential field function can be expressed as

$$U_{\text{total}}(q) = U_{\text{att}}(q) + U_{\text{rep}}(q) + U_{\text{heat-rep}}(q) \tag{23}$$

Gradient descent is used to find a path from the starting point to the target point in the total potential field.

$$q_{\text{next}} = q_{\text{current}} - \nabla * U_{\text{total}}(q_{\text{current}}) \tag{24}$$

The potential field coefficients k_{rep} and $k_{\text{heat-rep}}$ are adjusted to achieve a balance between obstacle avoidance and thermal constraints. Through the above method, the point cloud map based on thermal information and the artificial potential field method can be realized.

In the process of path generation based on the potential field method, although the introduction of the discretization step guarantees the convergence of the algorithm, it inevitably leads to the non-smooth oscillation of the path. This paper uses the Savitzky–Golay filter for path smoothing, which is a smoothing algorithm based on local polynomial fitting. The core idea is to preserve the characteristics of the signal by polynomial fitting in the sliding window while suppressing noise-induced fluctuations. The SG filter maintains the geometry of the signal while smoothing.

For the path sequence $Q = \{q_1, q_2, \ldots, q_n\}$, the polynomial is fitted in the sliding window, and the formula is as follows.

$$\begin{cases} x(t) = a_0 + a_1 t + a_2 t^2 + \cdots + a_k t^k \\ y(t) = b_0 + b_1 t + b_2 t^2 + \cdots + b_k t^k \end{cases} \tag{25}$$

where t is the local time coordinate in the window and k is the polynomial order. The coefficients $\{a_k\}$, $\{b_k\}$ are solved by the least square method, and the value of the fitting polynomial at the center point of the window is used as the smoothed output. The filtered coordinates can be expressed as

$$Q_{\text{smooth}} = SG_\text{Filter}(Q, k, w) \tag{26}$$

where k is the polynomial order, representing the highest degree of fitting the polynomial and w is the window size representing the sum of the current points used in each fit and the number of points before and after them. The smoothed path after fitting is shown in Figure 4.

https://doi.org/10.1017/S0263574725102774 Published online by Cambridge University Press

The pseudocode of the path-planning algorithm with thermal map is shown below.

Algorithm 1. *Temperature-enhanced Artificial Potential Field Path Planning.*

Input:
q_start, q_goal: Start and goal positions
Obstacle_List: List of obstacles with positions and temperatures
k, m, k_heat: Gain coefficients
ρ_0, T_threshold: Influence distance and temperature threshold
L: Step size
δ: Convergence threshold
max_iterations: Maximum number of iterations
α, β: Thermal repulsion parameters
Output:
Path: A sequence of points from q_start to q_goal
Path ← [q_start]
q_current ← q_start
for iter = 1 to max_iterations do
  if ||q_current - q_goal|| < δ **then**
    Path ← Path ∪ [q_goal]
    break
  end if
  F_att ← k · (q_goal - q_current) ▷ Step 1: Calculate attractive force
  F_rep_total ← 0
  for each obstacle in Obstacle_List do
    d ← ||q_current - q_obs|| ▷ Step 2 Calculate distance to obstacle
    if d ⩽ ρ_0 **then**
      F_rep_geo ← 0.5 • m • (1/d - 1/ρ_0)² • ||q_goal - q_current||² • ((q_current - q_obs) / d)
      F_rep_total ← F_rep_total + F_rep_geo ▷ Step 2.2: Add geometric repulsive force
    end if
    if T_obs ⩾ T_threshold **then**
      ρ_t ← -α · (ln(T_threshold) - ln(T_obs)) ▷ Step 2.3: Calculate thermal influence distance
      if d ⩽ ρ_t **then**
        k_heat_effective ← k_heat · (1 - exp(-β · d^0.1)) ▷ Step 2.4: Calculate effective thermal gain

https://doi.org/10.1017/S0263574725102774 Published online by Cambridge University Press

Algorithm 1. *(Continued)*

F_rep_thermal ← 0.5 • k_heat_effective • (T_obs - T_threshold) / d ² • ((q_current - q_obs) / d)
F_rep_total ← F_rep_total + F_rep_thermal ▷ Step 2.5: Add thermal repulsive force
end if
end if
end for
F_total ← F_att + F_rep_total ▷ Step 3: Calculate total force
if ||F_total|| > 0 **then**
q_next ← q_current + L · F_total / ||F_total|| ▷ Step 4.1: Move along force direction
else
q_next ← q_current + L · (rand(2) - 0.5) ▷ Step 4.2: Random move if zero force
end if
Path ← Path ∪ [q_next] ▷ Step 5: Update path
q_current ← q_next ▷ Step 6: Update current position
end for
return Path ▷ Step 7: Return final path

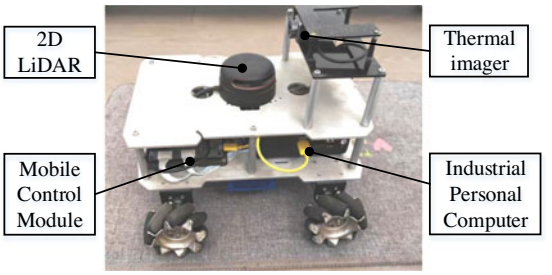


Figure 5. *The mobile robot platform.*

4. Case study

In this paper, the mobile robot platform based on the Ubuntu system is adopted. The platform is equipped with RPLIDAR-A2 LiDAR and Hikmicro thermal imager, which are shown in Figure 5.

4.1. Temperature-enhanced point cloud map

The thermal image obtained by the thermal imager and the point cloud data obtained by 2D LiDAR are, respectively, in their coordinate systems. The thermal image and 2D point cloud are shown in Figure 5 above.

The infrared thermal image with a resolution of 512 × 384 output by the thermal imager is shown in Figure 6(a). Each pixel contains radiation intensity information, which is converted into a temperature

https://doi.org/10.1017/S0263574725102774 Published online by Cambridge University Press

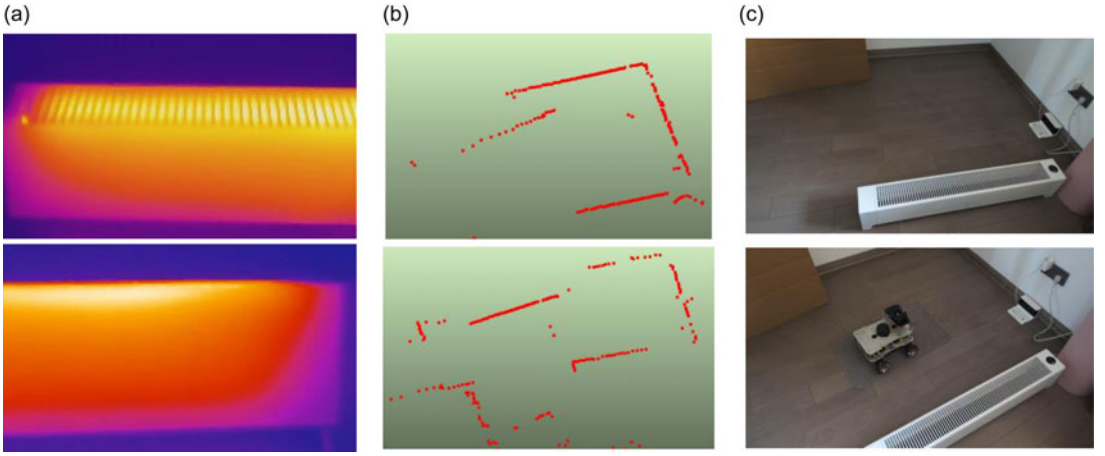


Figure 6. *Thermal images (a), 2D point clouds (b), and physical photo (c).*

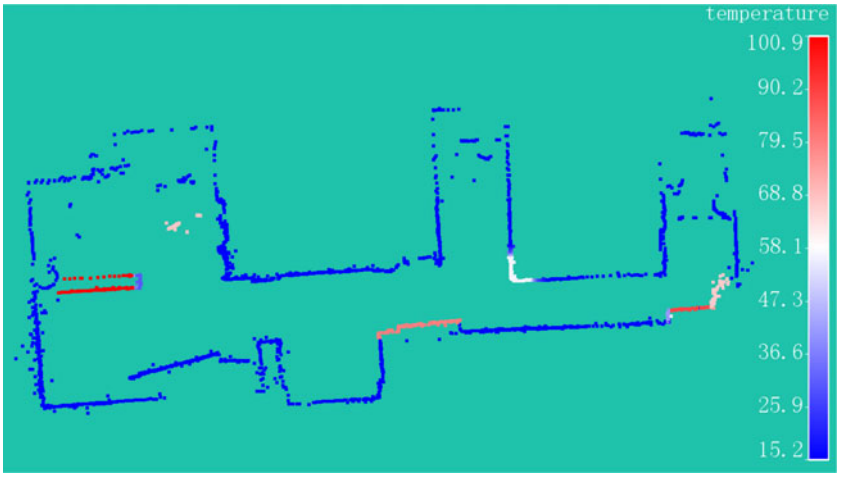


Figure 7. *Temperature-enhanced point cloud map. Point color depth corresponds to temperature value (dark red → high temperature, dark blue → low temperature).*

value according to parameters. The horizontal field of view Angle of the single-line LiDAR is 270°, and the angular resolution is 0.25°, as shown in Figure 6(b). The generated two-dimensional polar coordinate point cloud is expressed as $\{(r_i, \theta_i)(x_i, y_i)\}$ after Cartesian coordinate conversion.

After the joint calibration, the data of the two sensors are unified in a spatial coordinate system. The pixel information of the thermal image is converted into temperature information, and the temperature information of the thermal imager is embedded in the LiDAR point cloud to generate a two-dimensional temperature-enhanced point cloud map. After fusion, the point cloud format is (x, y, T). The two-dimensional temperature point cloud image after fusion is shown in Figure 7.

4.2. Improved artificial potential field method

To verify the robustness of the improved artificial potential field method based on temperature-enhanced point cloud maps in thermal environments, experiments were conducted in three typical scenarios:

1. Family-living environment: there are both localized high-temperature zones generated by heating appliances and thermal regions to mimic electrical overload scenarios. There are several fixed high-temperature points distributed in the environment ($T \approx 90$ °C).

https://doi.org/10.1017/S0263574725102774 Published online by Cambridge University Press

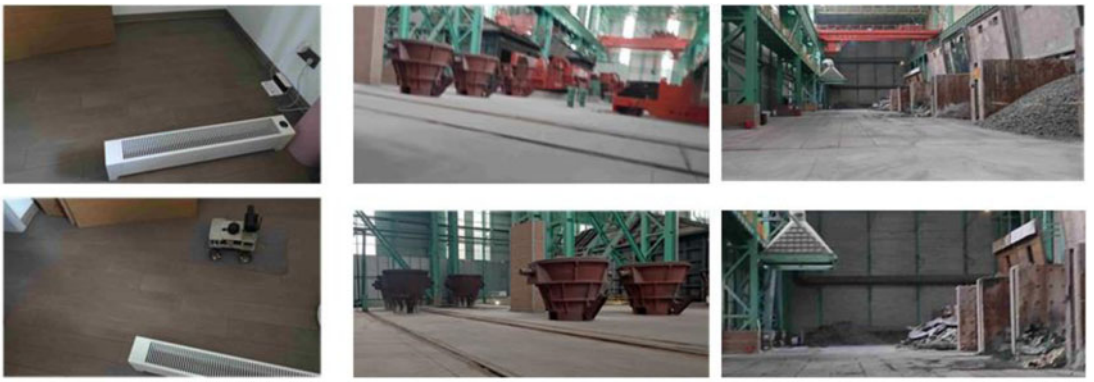


Figure 8. *Three scenarios: (1) family-living environment; (2) continuous casting workshop; (3) steelmaking scrap area.*

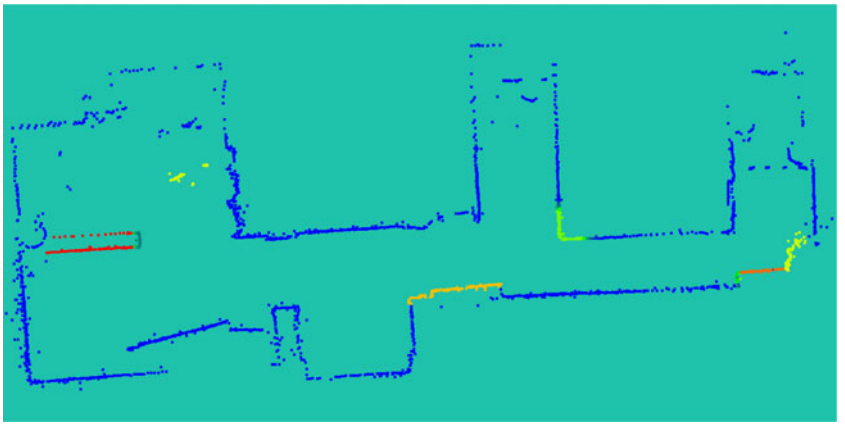


Figure 9. *Temperature-enhanced point cloud map in the family-living environment.*

2. Continuous casting workshop: there are several steelmaking furnaces with different high temperatures ($T > 100$°C).
3. Steelmaking scrap area: there are unstructured barriers to stacking metal waste ($T \in [50, 300]$°C).

The actual environment of these three scenarios is shown in Figure 8.

In scenario 1, the point cloud with temperature information is collected by the mobile robot, as shown in Figure 9 above. The heat source here is mainly electric heating, air heaters, and simulated overload electrical appliances.

Now the space is divided into grids, the temperature within each grid is averaged, and the repulsive force is calculated based on the grid. The goal is to reduce the amount of computation while reducing the impact of density. The attraction coefficient and repulsion coefficient are adjusted to adapt to the current environment.

Due to the hardware temperature requirements of each component of the robot, the threshold temperature T_{thre} is set at 40 °C. k_{att} represents the gravitational gain, which controls the magnitude of the attraction force exerted by the target point on the robot. The larger the value, the stronger the gravitational force, and the more "urgently'' the robot will head towards the target. k_{rep} is the basic repulsive force gain, which controls the magnitude of the repulsive force generated by ordinary obstacles (regardless of temperature). The larger the value, the more "repelled'' it is by the obstacle, and the path will be

https://doi.org/10.1017/S0263574725102774 Published online by Cambridge University Press

Table I. *The influence of parameters on performance indicators.*

Parameters	Scanning range	Expected impact
k_{att}	[0.5, 5]	Too small: slow convergence; too large: risk of traversing hazardous zones or causing oscillations
k_{rep}	[0.1, 1.0]	Too small: increased collision risk; too large: redundant path elongation or failure to reach the target
$k_{heat\text{-}rep}$	[0.001, 0.05]	Too small: inability to avoid high-temperature regions; too large: overly conservative path planning
β	[0.05, 0.5]	Too small: excessively smooth force field lacking detail; too large: abrupt changes in repulsive force leading to non-smooth paths

Table II. *Final parameters.*

Parameters	Values
k_{att}	2
k_{rep}	0.3
$k_{heat\text{-}rep}$	0.005
β	0.1

further away from the obstacle. Due to the introduction of the temperature repulsion force, k_{rep} should be smaller than the traditional APF. $k_{heat\text{-}rep}$ is the base value gain of the temperature-repulsive force. It controls the absolute intensity of the temperature-repulsive force. The larger the value, the stronger the additional repulsive force generated by the high-temperature obstacle. β is the temperature-repulsive force attenuation coefficient, which controls the rate at which the temperature-repulsive force decays with distance. The larger β is, the faster the attenuation is, and the more concentrated the influence range of the high-temperature-repulsive force is.

The single-parameter scanning analysis method is adopted. The traditional APF parameters are referenced, and one parameter is changed within a reasonable range. After fixing three parameters, multiple simulations are conducted to observe their impact on performance indicators, as shown in Table I.

Finally, the detailed parameter settings under scenario 1 are shown in Table II. The selected parameter values have been proven to achieve the best balance between path safety (minimizing high-temperature exposure) and path efficiency (shortest feasible length).

Based on the grid map, an improved artificial potential field method is used for path planning. As shown in Figure 10, under the combined action of attractive and repulsive forces, the planned path can successfully avoid the high-temperature heat source. The final generated path uses the Savitzky–Golay filter to smooth the planned path, as shown in Figure 11. The variation curves of attraction, repulsion, and resultant force with the increase of iterations are shown in Figure 12. Temperature repulsion plays an important role in planning.

To verify the performance of the algorithm in the scenario, 15 independent experiments were conducted to ensure the reliability of the results. The underlying geometric parameters (such as step length and obstacle influence distance) of the traditional APF and this improved method were kept consistent to fairly compare the performance gain after the introduction of the temperature field. The statistical results of multiple experiments and related performance indicators are recorded, and a comparison is made with the traditional APF, as shown in the table below (Table III).

Compared with the traditional APF, the improved method successfully reduced the working path temperature by 20% and significantly reduced the risk of high-temperature exposure, while the actual path length increased only slightly.

https://doi.org/10.1017/S0263574725102774 Published online by Cambridge University Press

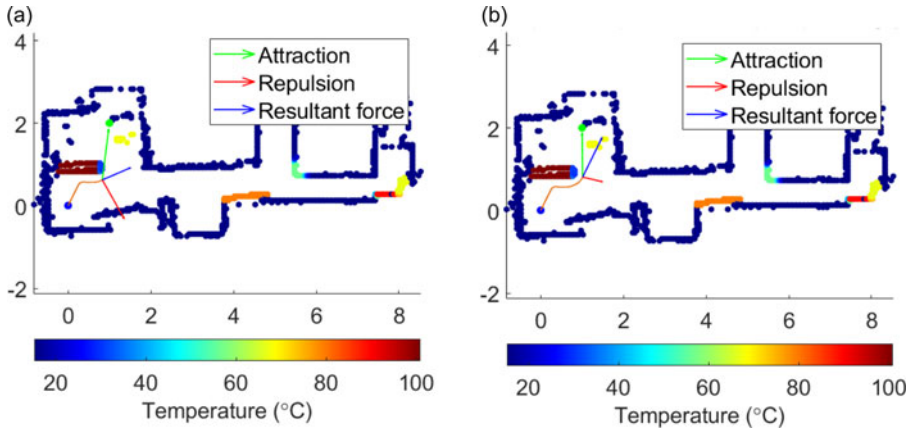


Figure 10. *Gridded temperature potential field path planning. The blue dot is the starting point, and the green dot is the end point. The green, red, and blue arrows represent attraction, repulsion, and resultant force, respectively.*

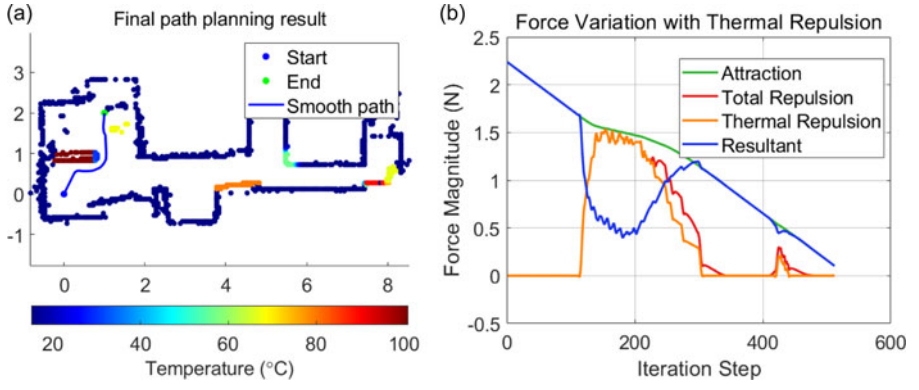


Figure 11. *Final path planning result and force variation with thermal repulsion.*

Change different starting and ending points for path planning. The resulting path and force diagram are shown in Figure 12.

Then, 15 independent experiments are conducted in the home environment. The statistical results of multiple experiments and related performance indicators are recorded, and a comparison is made with the traditional APF, as shown in Tables IV and V below.

The improved method successfully planned paths that completely avoided the core area of high temperature in all 15 trials, achieving almost 100% elimination of high-temperature exposure.

In scenario 2, the mobile robot collects the enhanced point cloud, as shown in Figure 13. The heat source here is mainly the converter steelmaking furnace with residual temperature.

Based on the grid map, an improved artificial potential field method is used for path planning. Under the combined action of attractive and repulsive forces, the planned path can successfully avoid the high-temperature heat source. The final generated path is shown in Figure 14. The variation curves of attraction, repulsion, and resultant force with the increase of iterations are shown in Figure 14. Considering the high temperature in the environment, the repulsive force in path planning is almost the only repulsive force of temperature.

Then, 15 independent experiments are conducted in the continuous casting workshop. The statistical results of multiple experiments and related performance indicators are recorded, and a comparison is made with the traditional APF, as shown in Tables VI and VII below.

https://doi.org/10.1017/S0263574725102774 Published online by Cambridge University Press

Table III. *Comparison of performance indicators for path planning in the family-living environment.*

Indicators	Traditional APF	Improved APF	Improvement rate (%)
Average path temperature (°C)	38.7 ± 2.5	29.8 ± 1.6	23
Maximum instantaneous temperature(°C)	51 ± 3.2	41.7 ± 2.5	18
Path temperature variance	126.8 ± 5.8	46.4 ± 3.5	63
High-temperature exposure distance(m)	1.2 ± 0.21	0.14 ± 0.2	88
Total path length(m)	2.73 ± 0.12	2.67 ± 0.08	2

Table IV. *Comparison of performance indicators for path planning in the family-living environment.*

Indicators	Traditional APF	Improved APF	Improvement rate (%)
Average path temperature (°C)	28.7 ± 2.5	25.3 ± 1.2	12
Maximum instantaneous temperature (°C)	42.5 ± 3.2	34.7 ± 2.5	18
Path temperature variance	28.8 ± 1.8	2.4 ± 0.5	92
High-temperature exposure distance (m)	0.56 ± 0.21	0 ± 0.00	100
Total path length (m)	5.22 ± 0.22	5.36 ± 0.15	−3

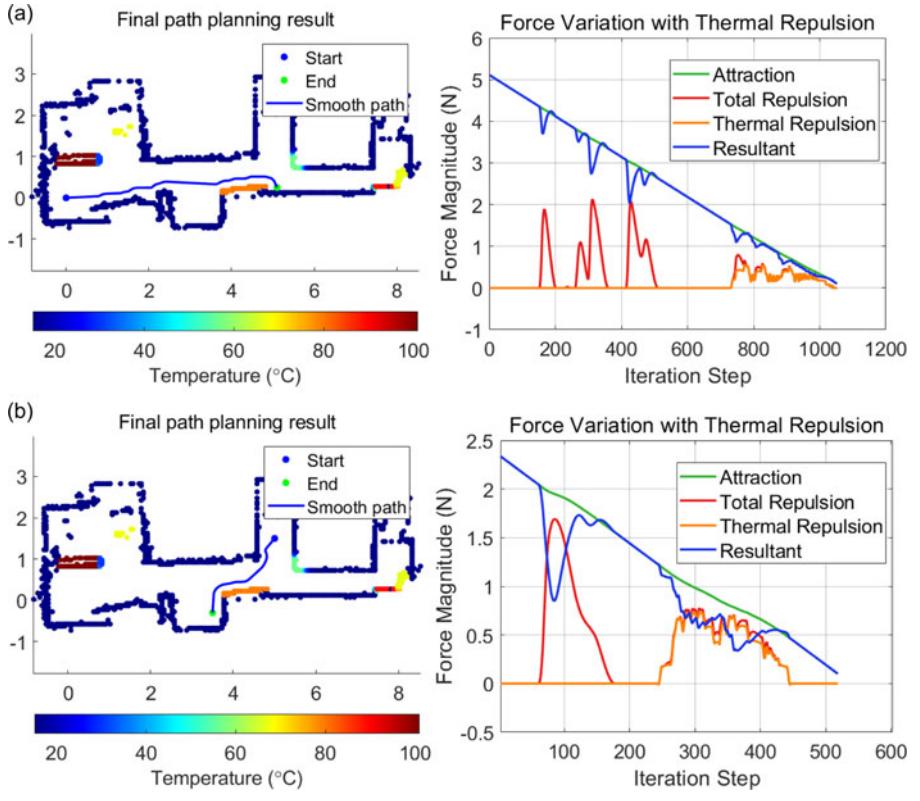


Figure 12. *Final path planning result and force variation of two different starting and ending points.*

https://doi.org/10.1017/S0263574725102774 Published online by Cambridge University Press

Table V. *Comparison of performance indicators for path planning in the family-living environment.*

Indicators	Traditional APF	Improved APF	Improvement rate (%)
Average path temperature (°C)	28.9 ± 2.4	25.2 ± 1.0	13
Maximum instantaneous temperature	41.6 ± 3.2	32.7 ± 2.5	23
Path temperature variance	30.26 ± 2.1	1.45 ± 0.3	95
High-temperature exposure distance	0.25 ± 0.15	0 ± 0.00	100
Total path length	2.53 ± 0.08	2.6 ± 0.08	−3

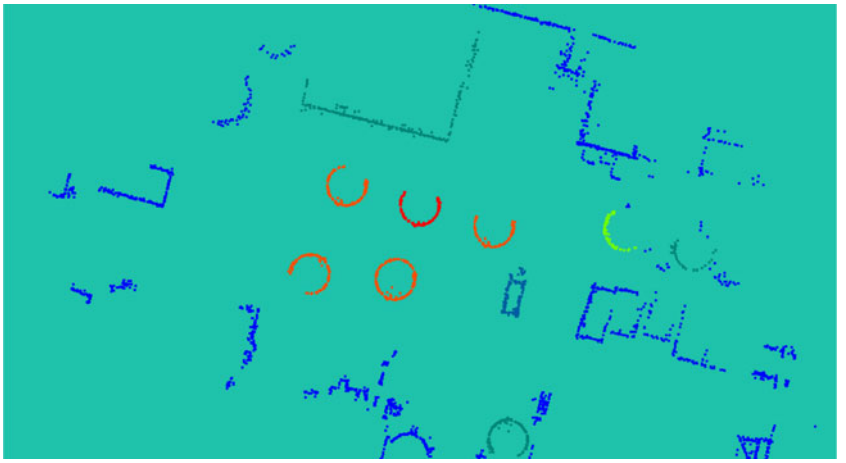


Figure 13. *Temperature-enhanced point cloud map in the continuous casting workshop.*

Compared to the traditional APF, the improved method successfully reduces the temperature of the working path in the factory environment by 50%-60% and greatly reduces the risk of high-temperature exposure, with a small and negligible increase in the actual path length.

In scenario 3, the mobile robot collects the enhanced point cloud, as shown in Figure 15. The heat source here is mainly waste from the steelmaking process.

Based on the grid map, an improved artificial potential field method is used for path planning. Under the combined action of attractive and repulsive forces, the planned path can successfully avoid the high-temperature heat source. The final generated path is shown in Figure 16. The variation curves of attraction, repulsion, and resultant force with the increase of iterations are shown in Figure 16. Considering the high-temperature waste in the environment, the repulsive force in path planning is almost the only repulsive force of temperature.

Fifteen independent experiments are conducted in the steelmaking scrap area. The statistical results of multiple experiments and related performance indicators are recorded, and a comparison is made with the traditional APF, as shown in Table VIII below.

In a larger environment, the modified method successfully reduced the operating path temperature by 40% and substantially reduced the risk of high-temperature exposure, with a modest increase in the actual path length.

The effectiveness and robustness of the improved artificial potential field method based on temperature-enhanced point cloud map in thermal environment path planning are proved through the experimental verification of three typical scenarios: home life, continuous casting workshop, and steelmaking waste area. Experiments show that the algorithm can effectively avoid local high-temperature sources and generate safe and smooth paths in both structured and unstructured environments. In high-temperature industrial scenarios, the temperature repulsion contribution accounts for the main

https://doi.org/10.1017/S0263574725102774 Published online by Cambridge University Press

Table VI. *Comparison of performance indicators for path planning in the continuous casting workshop.*

Indicators	Traditional APF	Improved APF	Improvement rate (%)
Average path temperature (°C)	74.2 ± 3.6	32.8 ± 1.3	56
Maximum instantaneous temperature	116.3 ± 4.2	55.6 ± 2.5	52
Path temperature variance	12,185.7 ± 80.1	239.6 ± 6.1	98
High-temperature exposure distance	19.32 ± 1.34	4.86 ± 0.35	75
Total path length	26.33 ± 1.83	28.98 ± 2.01	−10

Table VII. *Comparison of performance indicators for path planning in the continuous casting workshop.*

Indicators	Traditional APF	Improved APF	Improvement rate (%)
Average path temperature (°C)	84.2 ± 3.9	32.1 ± 1.3	62
Maximum instantaneous temperature	117.3 ± 4.2	54.3 ± 2.3	54
Path temperature variance	12,785.7 ± 83.2	256.2 ± 6.8	98
High-temperature exposure distance	22.42 ± 2.36	5.73 ± 0.37	74
Total path length	30.32 ± 1.86	33.1 ± 2.25	−9

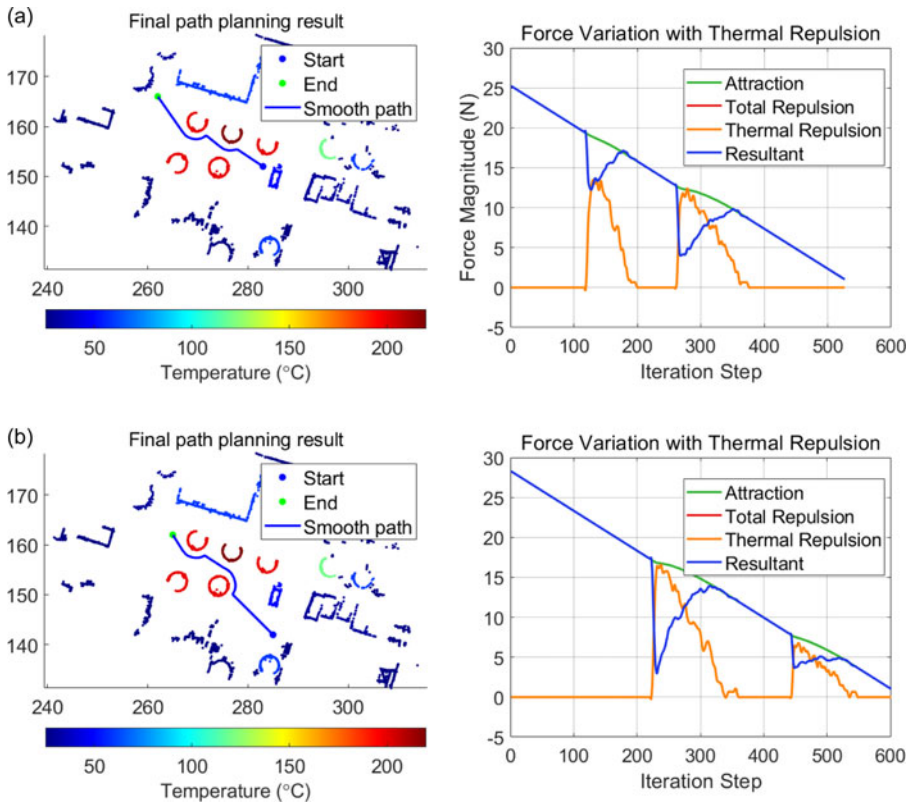


Figure 14. *Final path planning result and force variation of two different starting and ending points.*

https://doi.org/10.1017/S0263574725102774 Published online by Cambridge University Press

Table VIII. *Comparison of performance indicators for path planning in the steelmaking scrap area.*

Indicators	Traditional APF	Improved APF	Improvement rate (%)
Average path temperature (°C)	54.2 ± 2.0	32.1 ± 1.5	41
Maximum instantaneous temperature	116.3 ± 4.2	53.8 ± 2.3	53
Path temperature variance	18,785.7 ± 93.6	356.2 ± 9.2	98
High-temperature exposure distance	32.42 ± 2.36	5.73 ± 0.22	82
Total path length	77.12 ± 2.87	82.52 ± 2.99	−7

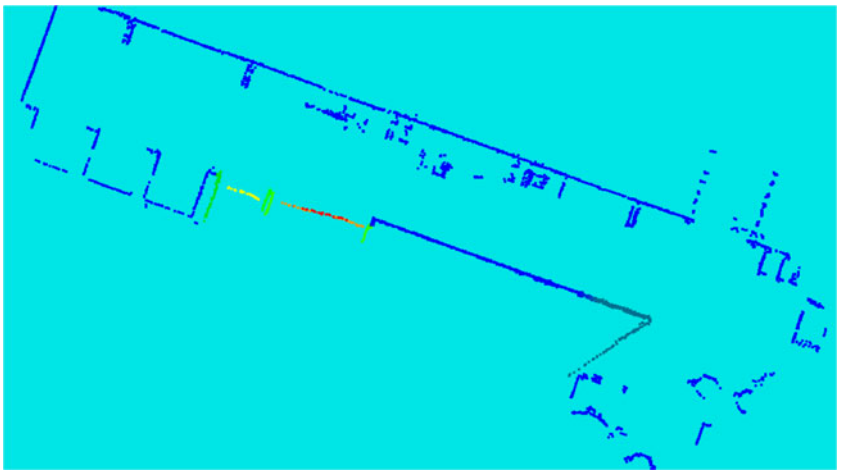


Figure 15. *Temperature-enhanced point cloud map in the steelmaking scrap area.*

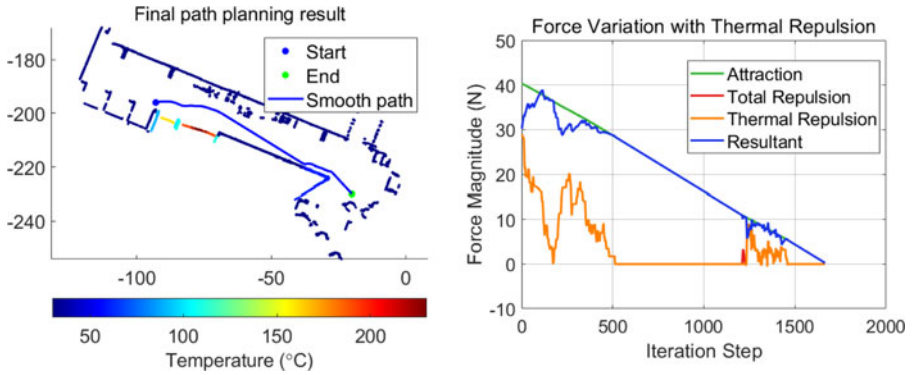


Figure 16. *Final path planning result and force variation with thermal repulsion.*

proportion and becomes the main driving force for obstacle avoidance. Compared with the traditional APF method, the improved method successfully reduces the operating path temperature by 20–60%, and greatly reduces the risk of high-temperature exposure, which verifies the necessity of the thermal environment potential field model.

4.3. Discussion

There still exist many works worthy of further investigation. Only the feasibility of avoiding high temperatures is considered, and how to determine the repulsive force for different heat sources needs further

https://doi.org/10.1017/S0263574725102774 Published online by Cambridge University Press

study. This planning method does not analyze the avoidance of dynamic heat sources and the transient change of the temperature field.

Based on these problems, the following research can be conducted from the following aspects. Parameters based on deep reinforcement learning are considered to be adaptive to different environments. Then, the existing model is improved to enhance the real-time performance of the algorithm.

5. Conclusion

This paper presents an improved potential field method for the path planning of mobile robots in thermal environments based on temperature-enhanced point cloud maps. This paper presents an improved potential field method for the path planning of mobile robots in thermal environments based on temperature-enhanced point cloud maps. The temperature-enhanced point cloud map is generated by combining LiDAR and thermal imaging, and the repulsive potential field function of heat radiation is introduced to realize robot path planning based on the traditional artificial potential field method. The reliability of the proposed method is verified by collecting environmental data and conducting experiments. This study provides a new idea for robot autonomous navigation under high-temperature and high-risk environments.

In the future, the direction of our next work will adopt 3D LiDAR instead of 2D LiDAR and inherit the fusion framework of this paper. It will be investigated how thermal textures can be effectively mapped onto 3D point clouds to construct a fully 3D fusion map and enable path planning. The grid map framework for probabilistic heat occupancy is adopted to consider further, and a novel method of adding heat data to update rules will be developed to improve the current method. Dynamic temperature field prediction and multi-sensor information will be further integrated to cope with more complex time-varying thermal environment challenges.

Data availability statement. The data that support the findings of this study are available from the corresponding author upon reasonable request.

Authors contribution. Yunzhi Li: Conceptualization, Methodology, Writing – original draft, Writing – review and editing; Libin Tan: Conceptualization, Writing – review and editing; Xiangrong Xu: Writing – review and editing; Zequn Zhang: Funding acquisition. All authors had approved the final version.

Financial support. This work was supported by the National Natural Science Foundation of China (52305539), the Natural Science Foundation of Jiangsu Province (BK20230880), and the China Postdoctoral Science Foundation (2023M731661).

Competing interests. The authors declare that they have no known competing financial interests or personal relationships that could have appeared to influence the work reported in this paper.

Ethical and informed consent for data used. This paper was done by the authors, and no human participants other than the authors were involved in it, and informed consent was obtained from all authors.

References

[1] O. Lara-Guzmán, S. A. Serrano, D. Carrillo-López and L. E. Sucar, "RGB-D Camera and 2D Laser Integration for Robot Navigation in Dynamic Environments," **In:** *Advances in Soft Computing, Lecture Notes in Computer Science* (L. Martínez-Villaseñor, I. Batyrshin and A. Marín-Hernández, eds.), vol. 11835 (Springer International Publishing, Cham, 2019) pp. 661–674. doi: 10.1007/978-3-030-33749-0_53.

[2] L. Liu, X. Wang, X. Yang, H. Liu, J. Li and P. Wang, "Path planning techniques for mobile robots: Review and prospect," *Expert Syst. Appl.* **227**, 120254 (2023). doi: 10.1016/j.eswa.2023.120254.

[3] A. Loganathan and N. S. Ahmad, "A systematic review on recent advances in autonomous mobile robot navigation," *Eng. Sci. Technol., Int. J.* **40**, 101343 (2023). doi: 10.1016/j.jestch.2023.101343.

[4] R. Frikha, R. Ejbali and M. Zaied, "Camera pose estimation for augmented reality in a small indoor dynamic scene," *J. Electron. Imaging* **26**(05), 1 (2017). doi: 10.1117/1.JEI.26.5.053029.

https://doi.org/10.1017/S0263574725102774 Published online by Cambridge University Press

[5] Y. Lu and G. Lu, "An Alternative of LiDAR in Nighttime: Unsupervised Depth Estimation Based on Single Thermal Image," **In:** *IEEE Winter Conference on Applications of Computer Vision (WACV)* (IEEE, Waikoloa, 2021) pp. 3832–3842. doi: 10.1109/WACV48630.2021.00388.
[6] S. Rho, S. M. Park, J. Pyo, M. Lee, M. Jin and S.-C. Yu, "LiDAR-stereo thermal sensor fusion for indoor disaster environment," *IEEE Sens. J.* **23**(7), 7816–7827 (2023). doi: 10.1109/JSEN.2023.3245619.
[7] L. Douadi, Y. Dupuis and P. Vasseur, "Stable keypoints selection for 2D LiDAR based place recognition with map data reduction," *Robotica* **40**(11), 3786–3810 (2022). doi: 10.1017/S0263574722000613.
[8] W. Chen, Y. Wang, H. Chen and Y. Liu, "EIL-SLAM: Depth-enhanced edge-based infrared-LiDAR SLAM," *J. Field Robot.* **39**(2), 117–130 (2022). doi: 10.1002/rob.22040.
[9] P. Wei, K. Fu, J. Villacres, T. Ke, K. Krachenfels, C. R. Stofer, N. Bayati, Q. Gao, B. Zhang, E. Vanacker and Z. Kong, "A compact handheld sensor package with sensor fusion for comprehensive and robust 3D mapping," *Sensors* **24**(8), 2494 (2024). doi: 10.3390/s24082494.
[10] I. Mantegh, M. R. M. Jenkin and A. A. Goldenberg, "Path planning for autonomous mobile robots using the boundary integral equation method," *J. Intell. Robot. Syst.* **59**(2), 191–220 (2010). doi: 10.1007/s10846-010-9394-y.
[11] W. Zhang, S. Wei, J. Zeng and N. Wang, "Multi-UUV path planning based on improved artificial potential field method," *Int. J. Robot. Autom.* **36**(4), 23–33 (2021). doi: 10.2316/J.2021.206-0531.
[12] X. Tong, S. Yu, G. Liu, X. Niu, C. Xia, J. Chen, Z. Yang and Y. Sun, "A hybrid formation path planning based on A* and multi-target improved artificial potential field algorithm in the 2D random environments," *Adv. Eng. Inform.* **54**, 101755 (2022). doi: 10.1016/j.aei.2022.101755.
[13] W. Chen, J. Sun, Z. Zhao and Q. Zheng, "Gaussian processes in polar coordinates for mobile robot using SE(2)-3D constraints," *J. Intell. Robot. Syst.* **103**(4), 72 (2021). doi: 10.1007/s10846-021-01520-0.
[14] S. Jia, C. Liu, H. Wu, D. Zeng and M. Ai, "A cross-correction liDAR SLAM method for high-accuracy 2D mapping of problematic scenario," *Isprs J. Photogram.* **171**, 367–384 (2021). doi: 10.1016/j.isprsjprs.2020.11.004.
[15] Z. Yuan, Q. Wang, K. Cheng, T. Hao and X. Yang, "SDV-LOAM: Semi-direct visual–LiDAR odometry and mapping," *IEEE Trans. Pattern Anal. Mach. Intell.* **45**(9), 11203–11220 (2023). doi: 10.1109/TPAMI.2023.3262817.
[16] X. Duan, Q. Hu, P. Zhao and S. Wang, "A low-cost and portable indoor 3D mapping approach using biaxial line laser scanners and a one-dimension laser range finder integrated with microelectromechanical systems," *photogram. Eng. Remote Sens.* **88**(5), 311–321 (2022). doi: 10.14358/PERS.21-00037R2.
[17] W. Ali, P. Liu, R. Ying and Z. Gong, "A feature based laser SLAM using rasterized images of 3D point cloud," *IEEE Sens. J* **21**(21), 24422–24430 (2021). doi: 10.1109/JSEN.2021.3113304.
[18] M. Pierzchała, P. Giguère and R. Astrup, "Mapping forests using an unmanned ground vehicle with 3D LiDAR and graph-SLAM," *Comput. Electron. Agric.* **145**, 217–225 (2018). doi: 10.1016/j.compag.2017.12.034.
[19] D. De Pazzi, M. Pertile and S. Chiodini, "3D radiometric mapping by means of LiDAR SLAM and thermal camera data fusion," *Sensors* **22**(21), 8512 (2022). doi: 10.3390/s22218512.
[20] H. Shin and K. Na, "Anomaly Detection using Elevation and Thermal Map for Security Robot,"**In:***2020 International Conference on Information and Communication Technology Convergence (ICTC)* (IEEE, Jeju, 2020) pp. 1760–1762. doi:10.1109/ICTC49870.2020.9289470.
[21] A. K. Krishnan, Methods for calibration, registration, and change detection in robot mapping applications (2016).
[22] O. Montiel, U. Orozco-Rosas and R. Sepúlveda, "Path planning for mobile robots using bacterial potential field for avoiding static and dynamic obstacles," *Expert Syst. Appl.* **42**(12), 5177–5191 (2015). doi: 10.1016/j.eswa.2015.02.033.
[23] Y. Rasekhipour, A. Khajepour, S.-K. Chen and B. Litkouhi, "A potential field-based model predictive path-planning controller for autonomous road vehicles," *IEEE Trans. Intell. Transp. Syst.* **18**(5), 1255–1267 (2017). doi: 10.1109/TITS.2016.2604240.
[24] M. Sun, X. Xiao, T. Luan, X. Zhang, B. Wu and L. Zhen, "The path planning algorithm for UUV based on the fusion of grid obstacles of artificial potential field," *Ocean Eng.* **306**, 118043 (2024). doi: 10.1016/j.oceaneng.2024.118043.
[25] C. Cui, S. Wu and X. Chen, "QuatAPF: Safety-aware and energy-efficient dynamic path planning and tracking control for deep-sea mining vehicles via a quatre-artificial potential field method," *Ocean Eng.* **321**, 120236 (2025). doi: 10.1016/j.oceaneng.2024.120236.
[26] Z. Pan, C. Zhang, Y. Xia, H. Xiong and X. Shao, "An improved artificial potential field method for path planning and formation control of the multi-UAV systems," *IEEE Trans. Circuits Syst.* **69**(3), 1129–1133 (2022). doi: 10.1109/TCSII.2021.3112787.
[27] H. Wu, Y. Zhang, L. Huang, J. Zhang, Z. Luan, W. Zhao and F. Chen, "Research on vehicle obstacle avoidance path planning based on APF-PSO," *Proc. Inst. Mech. Eng., Part D: J. Automob. Eng.* **237**(6), 1391–1405 (2023). doi: 10.1177/09544070221088364.
[28] Q. Ma, M. Li, G. Huang and S. Ullah, "Overtaking path planning for CAV based on improved artificial potential field," *IEEE Trans. Veh. Technol.* **73**(2), 1611–1622 (2024). doi: 10.1109/TVT.2023.3314860.
[29] X. Gu, L. Liu, L. Wang, Z. Yu and Y. Guo, "Energy-optimal adaptive artificial potential field method for path planning of free-flying space robots," *J. Frankl. Inst.* **361**(2), 978–993 (2024). doi: 10.1016/j.jfranklin.2023.12.039.
[30] Z. Liu, X. Yuan, G. Huang, W. Tan and Y. Wang, "3D gradient reconstruction-based path planning method for autonomous vehicle with enhanced roll stability," *IEEE Trans. Intell. Transp. Syst.* **23**(11), 20563–20571 (2022). doi: 10.1109/TITS.2022.3177608.

https://doi.org/10.1017/S0263574725102774 Published online by Cambridge University Press

[31] Z. Fan, F. Liu, X. Ning, Y. Han, J. Wang, H. Yang and L. Liu, "Improved *Q* -learning method for multirobot formation and path planning with concave obstacles," *J. Sens.* **2021**(1), 4294841 (2021). doi: 10.1155/2021/4294841.
[32] L. Cao, L. Wang, Y. Liu and S. Yan, "3D trajectory planning based on the rapidly-exploring random tree – Connect and artificial potential fields method for unmanned aerial vehicles," *Int. J. Adv. Robot. Syst.* **19**(5), 172988062211188 (2022). doi: 10.1177/17298806221118867.

Cite this article: Y. Li, L. Tan, X. Xu and Z. Zhang (2026). "Thermal point cloud-enhanced potential field path planning for mobile robots in high-temperature environments", Robotica **44**, 965–987. https://doi.org/10.1017/S0263574725102774

https://doi.org/10.1017/S0263574725102774 Published online by Cambridge University Press